

1 **Synchronization of great subduction megathrust earthquakes: Insights from scale model**
2 **analysis**

3 Matthias Rosenau¹, Illia Horenko², Fabio Corbi^{3,4}, Michael Rudolf¹, Ralf Kornhuber⁵, Onno
4 Oncken¹

5 ¹Helmholtz Centre Potsdam, GFZ German Research Centre for Geosciences, Potsdam,
6 Germany

7 ²Università della Svizzera italiana, Lugano, Switzerland

8 ³University RomaTre, Rome, Italy

9 ⁴University Montpellier, Montpellier, France

10 ⁵Freie Universität Berlin, Berlin, Germany

11

12

13

14

15

Pre-print

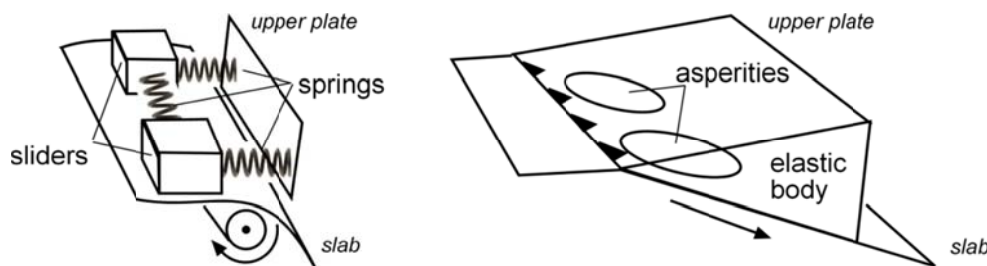
16 Abstract

17 The size of great subduction megathrust earthquakes is controlled mainly by the number of
18 adjacent asperities failing synchronously and the resulting rupture length. Here we investigate
19 experimentally the long-term recurrence behavior of a pair of asperities coupled by quasi-
20 static stress transfer over hundreds of seismic cycles. We statistically analyze long (c. 500 ka)
21 time-series of M8-9 analogue earthquakes simulated using a seismotectonic scale model
22 approach with two aims: First, to constrain probabilistic measures (frequency-size
23 distribution, variability) useful for hazard assessment and, second, to relate them with
24 geometric observables (coseismic slip pattern, locking pattern). We find that the number of
25 synchronized failures (double events) relative to the number of individual failures (solo
26 events) as well as the coefficient of variation of recurrence intervals scale with the logarithm
27 of stress coupling between the asperities. Tighter packed asperities tend to recur more
28 periodically while more distant asperities show clustering. The probability of synchronized
29 failures is controlled to first order by geometrical relations (size and distance of asperities).
30 The effects of rheological properties are evident but it remains to be explored to which extent
31 they vary in nature and how sensitive the system is to those.

32 1. Introduction

33 Giant magnitude 9 earthquakes unzip up to 1000 km long segments of active plate margins.
 34 Such long ruptures include failure of several asperities. Pre-requisites to fail synchronously
 35 (or sequentially in short succession, i.e. within seconds) are a homogeneous high stress level
 36 along the margin (i.e. in a late interseismic stage in different segments of the megathrust) and
 37 a trigger for nucleation which might be very small depending on the state of synchronization.
 38 Ruff (1996) introduced the idea of synchronization of the seismic cycle “clocks” in
 39 subduction zones by static stress transfer leading to giant earthquakes. He developed and
 40 analyzed a simple mechanical model consisting of two frictional spring-sliders coupled by a
 41 spring as an analogon of a segmented subduction zone with segments interacting by means of
 42 stress coupling (Fig. 1). He hypothesized that while individual recurrence times may initially
 43 be different (controlled by the individual frictional strength and spring stiffness) stress
 44 coupling may introduce variability and cause synchronization over multiple seismic cycles..

45



46

47 **Figure 1:** The concept of stress coupling and synchronization in subduction zones by means of coupled spring
 48 sliders as depicted by Ruff (1996) and the modern transformation of the idea by means of asperities coupled by
 49 elastic stress transfer in an elastic medium.

50 In a modern view Ruff's (1996) idea is based on clock advances triggered by static (Coulomb)
 51 stress transfer between asperities embedded in an elastic medium (Figure 1).

52 The first to model such a system realistically were Kaneko et al. (2010). They came up with a
53 fully dynamic simulation of a pair of coseismically weakening asperities separated by a
54 coseismically strengthening barrier. This simulation demonstrated the role of the size and
55 rheology of the barrier in controlling rupture propagation across it. Because of the
56 computational costs of such numerical models, the lengths of the simulated earthquakes were
57 rather limited to few tens of cycles.

58 Here we realize those models by means of seismotectonic scale modelling (Rosenau et al.,
59 2017a) which allows a realistic simulation of comparatively long analogue earthquake
60 sequences with up to 500 individual events at a rather low experiment and time cost compared
61 to numerical simulation. We simulate a subduction zone forearc wedge in an archetypical
62 setup with two seismogenic asperities characterized by velocity-weakening and unstable
63 stick-slip frictional behavior. The asperities are surrounded by velocity-strengthening material
64 displaying stable creep and acting as a barrier to seismic slip. Stress coupling by means of
65 static Coulomb stress transfer is realistically implemented by the elastic wedge and quantified
66 using elastic dislocation modelling. While frictional and elastic properties are kept constant
67 we vary the relative position of the two asperities along strike and across strike allowing us to
68 explore the effects of variable stress coupling and strength contrasts between the two
69 asperities.

70 Our study complements and extends recent analogue models by Corbi et al. (2017) who tested
71 the geometric aspects of Kaneko et al. (2010) simulation using a seismotectonic scale model
72 similar to the one we use. They were able to verify experimentally the major role of the
73 geometric relation between the asperities in synchronization. While they were able to
74 reproduce both the numerical results by Kaneko et al. (2010) as well as the natural
75 observations from Japan, the significance of frictional properties remained unexplored by
76 Corbi et al. (2017).

77 Here we complement these studies first by providing an analogue model with a different set of
78 frictional properties compared to Corbi et al. (2017) to allow testing their significance more
79 specifically. Second, we introduce a strength contrast between the two asperities, a factor
80 which has not been tested experimentally or numerically so far. Third, we generated about 10
81 times longer analogue sequences (up to 0.5 Million years long including several hundreds of
82 M8-M9 events) allowing a more rigorous statistical analysis and more reliable tests for
83 statistical significance.

84 **2. Modelling and analysis methods**

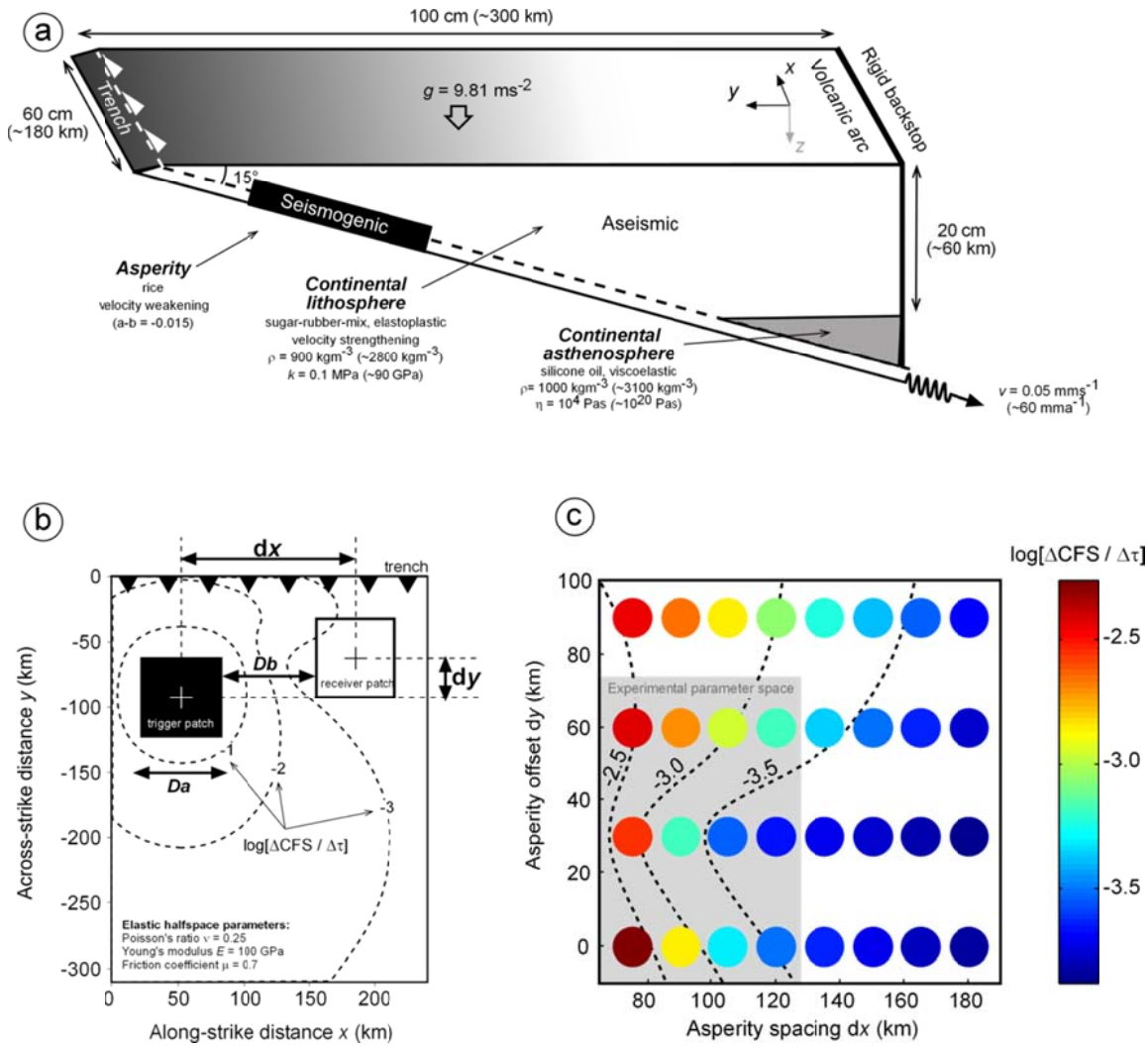
85 **2.1 Seismotectonic scale modelling of a subduction megathrust setting**

86 **2.1.2 Experimental setup and scaling**

87 Seismotectonic scale modelling is a cost-effective method to simulate long earthquake
88 sequences in a fully three-dimensional, dynamic and spatiotemporally quasi-continuous
89 framework (e.g. Rosenau et al. 2009, 2017, Corbi et al., 2013, 2017, Caniven et al. 2015,
90 2017). Here we recall the basics of the approach and report modifications specific to the
91 present study.

92 The experimental setup used in this study is a development from an earlier quasi-two-
93 dimensional setup used for seismotectonic scale modelling by Rosenau et al. (2009, 2010)
94 where the method has been explained in detail. The setup used in the current study is six-
95 times wider and therefore truly 3D and allows simulating along-strike rupturing of analogue
96 earthquakes. The experimental device consists of a glass-sided box (100 cm across strike, 60
97 cm along strike and 50 cm deep) with a 15° dipping basal conveyer plate on top of which a
98 compressive wedge (subduction forearc model) is set up at appropriate scale and compressed
99 against a rigid and fixed backwall (Figure 2a).

100



101

102 **Figure 2:** Seismotectonic scale model setup: (a) 3D view of analogue model setup (cross-section corresponds to
 103 $x = 50$ km in (b)); (b) Map-view (surface projection) of megathrust setup with calculated Coulomb stress
 104 changes $dCFS$ (normalized to stress drop $d\tau$ on trigger asperity) indicated (note the logarithmic fall-off with
 105 distance from the trigger asperity). D_a and D_b refer to the parameters used by Corbi et al. (2017). (c) Parameter
 106 space: Asperity spacing (dx) and offset (dy) and corresponding stress coupling $\log(dCFS/d\tau)$ in color and
 107 isolines. Grey shaded area corresponds to the subspace realized experimentally. Size of the asperities has not
 108 been changed in this study.

109 Dynamic similarity of the laboratory scale model with the natural prototype requires the ratios
 110 of forces, which are expressed as dimensionless numbers, to be the same as in nature. We use
 111 the following set of dimensionless numbers to ensure similarity with respect to strength σ ,
 112 gravity G , and inertia I :

113 1. The ratio τ between gravitation and strength (either elastic, frictional or viscous) is

$$114 \quad \tau = \rho \cdot l \cdot g / \sigma \quad (1)$$

115 where ρ is the rock density, l is a characteristic length, g is the gravitational acceleration, and

116 σ is the elastic, frictional or viscous strength.

117 2. The *Froude Number* Fr relates gravitation and inertia and is

$$118 \quad Fr = v \cdot (g \cdot l)^{-0.5} \quad (2)$$

119 where v is a characteristic velocity.

120 3. The *Cauchy Number* Ca relates inertia and elasticity and is

$$121 \quad Ca = \rho v^2 / k \quad (3)$$

122 where k is the bulk modulus.

123 By keeping these dimensionless numbers the same in an experiment executed in the earth's
124 gravity field as in nature, the following scaling relationships are derived from equations (1) to
125 (3):

$$126 \quad \tau^* = \tau \rightarrow (\sigma^*/\sigma) = (\rho^*/\rho) \cdot (l^*/l) \quad (4)$$

$$127 \quad Fr^* = Fr \rightarrow (t^*/t) = (l^*/l)^{0.5} \quad (5)$$

$$128 \quad Ca^* = Ca \rightarrow (k^*/k) = (\rho^*/\rho) \cdot (l^*/l)^2 \cdot (t/t^*)^2 \quad (6)$$

129 where “*” marks the model numbers and values. The ratios between model and natural
130 prototype values are known as the scaling factors [Hubbert, 1937].

131 These scaling relationships dictate the experimental conditions and material properties (Tab.
132 1) for a given length scale and material density. The model materials used here are three times
133 less dense and designed at a length scale $(l^*/l) = 3.3 \cdot 10^{-6}$ such that 1 cm in the scale model
134 corresponds to 3 km in nature. According to equations (4) – (6) it follows that the scale model

135 has to be weaker than the natural prototype by a factor $(\sigma^*/\sigma) = 1.1 \cdot 10^{-6}$ and should deform
136 ~ 500 times slower during analogue earthquakes in order to properly scale the body forces.
137 The corresponding coseismic time scale is $(t^*/t) = 1.8 \cdot 10^{-3}$ (i.e. 0.1 second in the lab
138 corresponds to about 50 seconds in nature). Because this dynamic time scale would result in
139 unsuitable long recurrence intervals of analogue earthquakes in the laboratory and because
140 inertial forces can be neglected during the quasi-static inter-event time we scale the
141 interseismic periods with a factor derived from the ratio of the viscosity scale and the stress
142 scale ($1.3 \cdot 10^{-10}$; 1 second in the lab scales to ~ 250 years).

143 Note that scale models represent strong simplifications of the natural prototype and their
144 application is always limited. See Rosenau et al. (2017) for a review of the seismotectonic
145 scale modelling approach.

146 **2.1.2 Scale model configuration and material properties**

147 The generalized subduction zone model presented here is analogous to a 300-km-wide and
148 180 km long forearc section from the trench to the volcanic arc (Figure 2a). The scale model
149 is made up of a granular wedge of elastic-frictional plastic (elastoplastic) mixtures of EPDM
150 (ethylene propylene diene monomer) rubber pellets with refined sugar and flavored rice
151 representing the brittle forearc lithosphere. The wedge overlies silicone oil representing the
152 viscoelastic asthenosphere. We generalize the natural subduction geometry by considering a
153 planar, 15° -dipping megathrust between an upper plate made up of ~ 60 -km-thick lithosphere
154 and ~ 20 -km thick asthenosphere below the arc and an oceanic plate. The latter is represented
155 by a conveyor plate pulled constantly via a spring-loaded thrust pad at $50 \mu\text{m/s}$ simulating
156 plate convergence at a long-term rate of about 60 mm/a in nature.

157 The model megathrust is defined by a few millimeters wide shear zone which forms at the
158 base of the wedge (“subduction channel”, *Shreve and Cloos* [1986]). It is characterized by
159 rate- and state-dependent frictional behavior similar to nature [*Scholz*, 1998]. In particular, it

160 includes two patches (20 cm x 20 cm ~ 60 km x 60 km) displaying stick-slip deformation and
161 mimicking a pair of seismogenic asperities separated by an aseismic barrier. The friction rate-
162 parameter $a-b$ within the asperities, made up of rice, is ~ -0.015 . The barrier separating the
163 two asperities as well as up- and downdip regions of the asperities are characterized by
164 aseismic slip or stable sliding (creep) controlled by the velocity strengthening behavior ($a-b \sim$
165 $+0.015$) of frictional slip in sugar. Material properties of this seismotectonic scale model have
166 been documented in detail in Rosenau et al. [2009, 2017] and Rudolf et al. (2016) and are
167 reported in Table 1.

168 The two asperities have an along subduction zone strike center-to-center distance (hereafter
169 called spacing) dx and are a relative shift across subduction zone strike (hereafter called
170 offset) dy (Figure 2b). This configuration allows exploring the effects of stress coupling (as
171 defined below in section 2.2.2) as well as strength contrast. We define the latter as the shear
172 strength of the weaker (shallower) asperity 2 relative to the stronger (deeper) asperity 1:

$$173 \text{ Strength contrast} = \tau_2/\tau_1 \quad (7)$$

174 Strength contrast therefore ranges theoretically from close to 0 to 1. Note the somewhat
175 counter-intuitive effect that low strength contrasts are reflected by τ_2/τ_1 values. In total
176 12 configurations have been realized in which we vary the strength contrast from 0.6 to 1.0
177 and the stress coupling from a few ppm to percent (Fig. 2c). The experimental runs took place
178 under normal gravity conditions and in a dry room climate (22 – 23°C, 30 – 40 % humidity).

179

Parameters:				Similarity:							
Quantity	Symbol	Dimension {M,L,T}	Unit	Quantity	Model	Nature	Dimensionless number	Scaling factor			
Model kinematics	Length	l	L	[m]	coseismic slip	29 ± 12	μm	8.8 ± 3.6	m	$Fr = \frac{v' [g l]^{0.5}}{v'}$	$3.3 \cdot 10^{-6}$
	Velocity (interseismic)	v	L/T	[m/s]	plate velocity	50	$\mu\text{m/s}$	60	mm/a		$2.6 \cdot 10^4$
	Velocity (coseismic)	v'	L/T	[m/s]	rupture velocity	> 3	m/s	> 2	km/s	$Ca = \frac{g a'}{\rho v'^2 / k}$	$1.8 \cdot 10^{-3}$
	Gravitational acceleration	g	L/T ²	[m/s ²]		9.81	m/s^2	9.81	m/s^2	g/a'	1
	Coseismic slip acceleration	a'	L/T ²	[m/s ²]		0.6	m/s^2	0.6	m/s^2	g/a'	1
Material properties	Friction coefficient	μ			interseismic	0.7		0.7		φ	1
	Friction rate parameter	$a-b$			strengthening/weakening	+/- 0.015		+/- 0.015		$a-b$	1
	Cohesion	C	M/LT ²	[Pa]	lithosphere	10	Pa	9	MPa		$1.1 \cdot 10^{-6}$
	Bulk modulus	k	M/LT ²	[Pa]	lithosphere	0.1	MPa	90	GPa		$1.1 \cdot 10^{-6}$
	Viscosity	η	M/LT	[Pas]	asthenosphere	10^4	Pas	$7 \cdot 10^{19}$	Pas		$1.4 \cdot 10^{-16}$
	Density	ρ	M/L ³	[kg/m ³]	lithosphere / asthenosphere	900/1000	kg/m^3	2800/3000	kg/m^3		$3.3 \cdot 10^{-1}$
Forces	Gravitation	$G = \rho V g$	ML/T ²	[N]							$1.2 \cdot 10^{-17}$
	Inertia	$I = \rho V a$	ML/T ²	[N]							$1.2 \cdot 10^{-17}$
Energy	Seismic moment	$M_0 = k D A$	ML ² /T ²	[Nm]	seismic moment	3 ± 2	Nm	$7 \cdot 10^{22} \pm 5 \cdot 10^{22}$	Nm		$4 \cdot 10^{-23}$

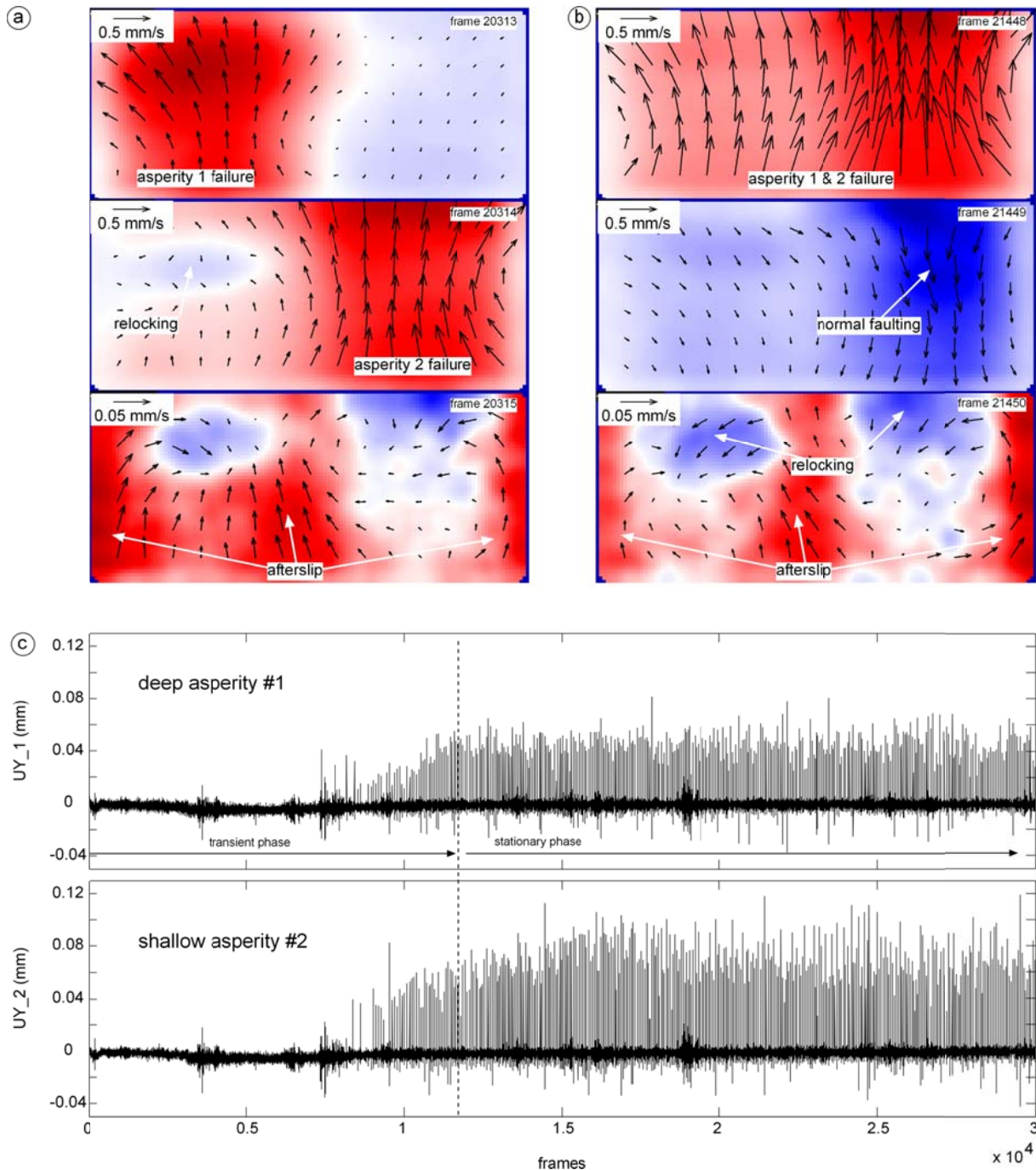
180

181 **Table 1:** Analogue model parameters, scaling relations and material properties182 **2.1.3 Experimental Monitoring and Strain Analysis**

183 For strain analysis of the evolving model wedges we use an optical image acquisition and
 184 correlation system (particle image velocimetry, PIV StrainMaster by LaVision, Germany, see
 185 *Adam et al. [2005]*, *Rosenau et al. [2009, 2010, 2017]* for applications in analogue tectonic
 186 and earthquake simulation).

187 During an experiment, the locations of particles on the model surface (i.e. within the x - y -plane
 188 of the model, Fig. 2) are recorded by sequential 11 Mpx-digital images of a 14-bit
 189 monochrome charge-coupled device (CCD) camera acquired at a frequency of 10 Hz. The x -
 190 y -displacement vector field between successive images is then determined by cross-
 191 correlation of textural differences (i.e. gray values) formed by groups of particles using a Fast
 192 Fourier Transform algorithm. The spatial resolution of the final displacement vector grid is \sim

193 3 mm or about 1 km in nature. For each grid-cell, an average x - z -displacement vector is
194 determined at micrometer precision (\sim decimeter scale in nature). This allows for observing
195 episodic surface deformation events corresponding to earthquakes of moment magnitude M_w
196 >8 . Analogue earthquakes are characterized by episodic, usually more than one order-of-
197 magnitude increased strain rates and a change in polarity of the wedge deformation from
198 “landward” motion (in negative y -direction) and compaction during the interseismic stage to
199 “seaward” motion and extension during the coseismic stage (Figure 3 a, b). Earthquakes
200 typically occur within a 0.1-second time interval, i.e. are captured by a solo image.



201
 202 **Figure 3:** Example of surface deformation pattern on top of the asperities (trench is north): (a) sequence of a
 203 cluster of two solo events followed by afterslip and reloading (each velocity field corresponds to 0.1 second
 204 experimental time). (b) sequence of a double event followed by a normal event, reloading and afterslip. Note the
 205 different vector scale for coseismic (upper, middle panel) and postseismic phases. Colors are scaled to the
 206 maximum velocity in each panel (red = surface displacement towards trench, white = 0, blue = away from the
 207 trench). (c) time-series of surface deformation towards the trench (UY) averaged over the surface projected area
 208 of asperity 1 and asperity 2 used for further analysis. Note the asymmetry in displacements above shallow and
 209 deep asperity which is related to the free-surface effect.

211 **2.2 Elastic dislocation modelling**

212 We use elastic dislocation modelling following Okada (1992) and Okada (1985) for
213 coseismic slip inversion and Coulomb stress transfer calculation employing the Matlab-based
214 software package “Coulomb” by Toda et al. (2011, Coulomb 3.3 Graphic-rich deformation
215 and stress-change software for earthquake, tectonic, and volcano research and teaching—user
216 guide: U.S. Geological Survey Open-File Report 2011–1060, 63 p., available at
217 <http://pubs.usgs.gov/of/2011/1060>). The model setup for elastic modelling uses the scaled
218 values of geometric and mechanical parameters given by the analogue model.

219 **2.2.1 Slip inversion**

220 Surface deformation during analogue earthquakes as captured by PIV is converted into
221 coseismic slip along the megathrust using inversion factors derived by forward elastic
222 dislocation modelling. Accordingly we find the factors relating horizontal surface deformation
223 U_Y directly above the dislocation at depth to slip S along it to range between 0.2 and 0.5
224 depending non-linearly on the depth of dislocation (Figure A1). Shallow dislocations show
225 larger factors, i.e. are less attenuated. We do not aim at a formal inversion or distributed slip
226 modelling. Instead we consider here mean coseismic surface displacement over the projected
227 surface area of the asperity to be a valuable proxy for mean coseismic slip over the asperity at
228 depth.

229 **2.2.2 Stress coupling**

230 For quantifying the interaction by means of stress coupling between the asperities we follow
231 the principles of static Coulomb stress transfer (CFS) modelling as established by King et al.
232 (1994) Toda and Stein (2002) and Lin and Stein (2004).

233 The model setup for CFS modelling is such that we impose thrust slip on one asperity (trigger
234 asperity) and average the predicted CFS increase ($dCFS$) for thrust faulting on the receiver

235 asperity (Fig. 2a). We then define a parameter called stress coupling as the CFS increase
236 averaged over the receiver asperity normalized by the stress drop on the trigger asperity:

$$237 \text{ Stress coupling} = d\text{CFS}/d\text{Tau}. \quad (8)$$

238 In the present setup stress coupling is in the order of less than a ppm up to one percent similar
239 to nature. Stress coupling falls off exponentially with distance and varies non-linearly across-
240 strike of the megathrust as a function of asperity spacing (dx) and offset (dy, Fig. A2).

241 **2.3 Numerical analysis of surface deformation time series**

242 Experimental time-series of surface deformation consist of typically a sequence of 30.000
243 images and corresponding incremental vector fields. To detect analogue earthquakes from
244 such a big data set we usually rely on computational algorithms sensitive to accelerations
245 validated by visual inspection. However, because of experimental noise such a kinematic
246 approach based on thresholding velocity usually has a high detection limit. Instead of
247 thresholding velocities to detect earthquakes stages we here employ a numerical time-series
248 analysis technique developed in computational statistics. This allows us to detect events
249 which can be below the detection threshold of classical kinematic approaches.

250 As input we use the surface deformation time-series of mean across-strike velocities $UY_1(t)$
251 and $UY_2(t)$ in the surface projection area of the two asperities (Figure 3c). Those data
252 typically show a transient phase without much activity in the beginning which reflects
253 stress buildup and reorganization within the analogue model (Figure 3c). After about 5.000-
254 10.000 increments (500-1000 seconds) surface accelerations reflecting analogue earthquakes
255 start to occur with increasing size and frequency and quickly reach a quasi-stationary state.
256 We use observations from this quasi-stationary state for further analysis.

257 To analyze the obtained experimental time series, we deploy a nonparametric time series
258 analysis methodology called Finite-Element-Method with Bounded Variation of model
259 parameters (FEM-BV) (Horenko 2009, Horenko 2010, Metzner et. al. 2012). Although it is
260 computationally more expensive than the common methods, FEM-BV has several important
261 conceptual advantages that were recently illustrated for various time series analysis
262 applications in geosciences (Vercauteren et. al. 2015, Risbey et. al 2015, Franzke et. al. 2015,
263 Kaiser et. al. 2015, O’Kane et. al. 2016). This nonparametric method is automatized, does not
264 rely on any tunable user-defined parameters (like thresholds values for the event
265 identification) and allows to go beyond strong parametric assumptions (like linearity, Gauss
266 or Poisson distribution assumptions for observed densities, stationarity or Markovianity) –
267 assumptions that are a constitutive part of the more common statistical time series analysis
268 approaches like multilinear regression, Hidden Markov Models or clustering methods (e.g.
269 Shearer and Stark, 2012). Going beyond these assumptions is especially important since
270 analyzed data exhibits a strong regime-transition behavior, is non-stationary, non-Markovian
271 and non-Gaussian in the regimes. Moreover, defining ad hoc threshold values for the events
272 could potentially introduce a user-defined bias. We refer to Metzner et. al (2012) for
273 mathematical/statistical details of the FEM-BV methodology – as well as for its
274 computational comparison with more common time series analysis methodologies.

275 **2.4 Statistical analysis of analogue earthquake sequences**

276 Based on the long sequences of analogue earthquakes we explore the recurrence behavior and
277 its intrinsic variability by means of univariate and bivariate statistics.

278 A simple measure of probability, used by earlier studies as well, is the relative number of
279 events of a given character (e.g. solo events, double/synchronized events). To get further
280 insight into the statistics however, the present studies allows producing probability
281 distribution functions (pdf) of distinct event parameters. We here use the pdf of moment

282 magnitudes (Figure 4a and A3) to characterize the “Gutenberg-Richter” frequency-size
283 relationship. And we use the pdf of the recurrence interval time (Figure 4c and A3) to
284 differentiate between periodic and aperiodic (e.g. clustered) occurrence of events.
285 Moreover, we quantify variability of the seismic moment (M_0) and recurrence time (T_{rec}) by
286 calculating the associated coefficients of variation:

$$287 \quad CV = \text{standard deviation} / \text{mean}. \quad (9)$$

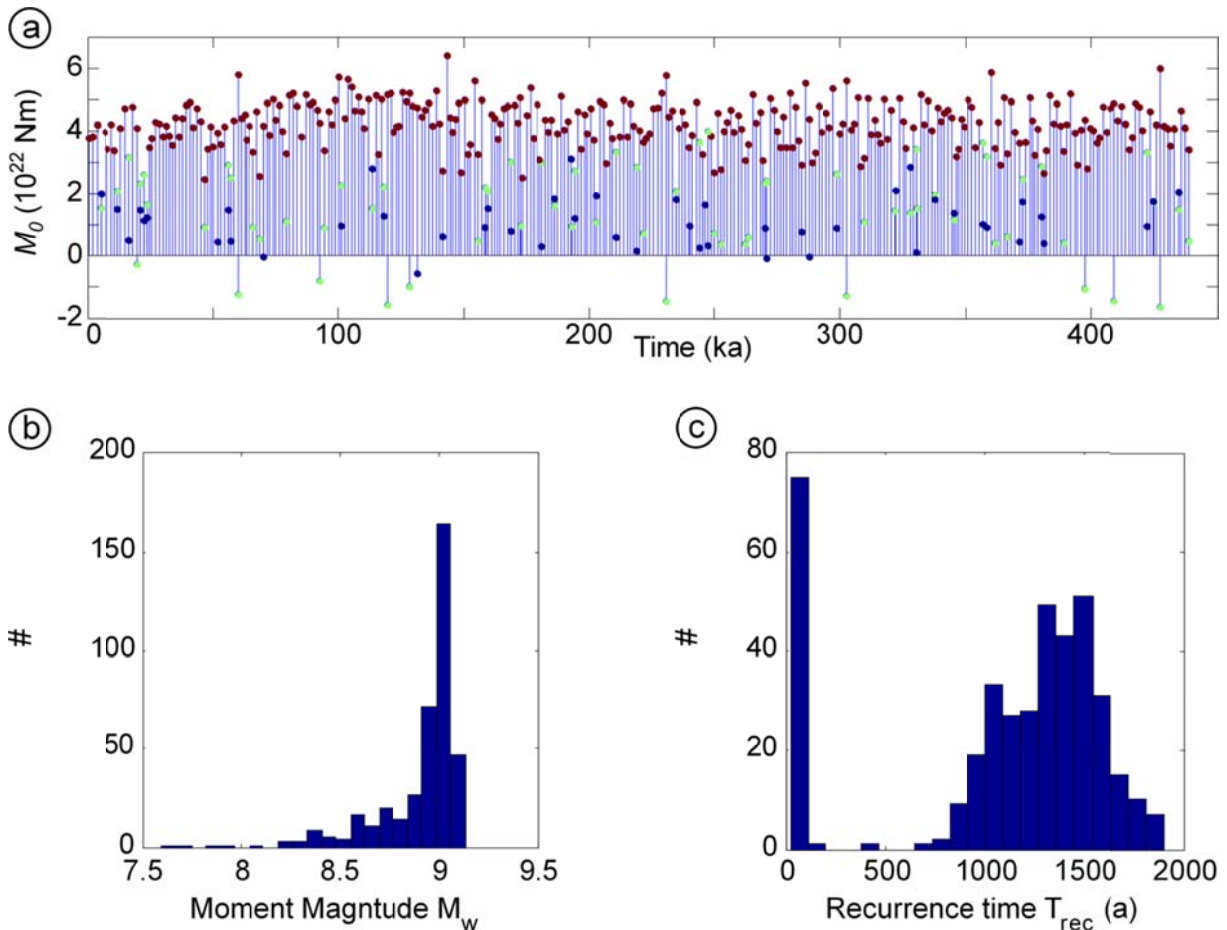
288 CV serves as a first-order proxy for recurrence behavior: a CV of 1 characterizes a random
289 behavior while $CV < 1$ suggests characteristic or periodic recurrence. A $CV > 1$ is characteristic
290 of clustering (e.g. Kuehn et al., 2008, Rosenau and Oncken, 2009).

291 **3 Experimental observations and interpretations**

292 **3.1 Seismic performance of the scale model**

293 A typical earthquake catalogue simulated by our scale model consist of up to 500 events of
294 moment magnitude 8-9 which occur over a time-period of about 500 ka (Fig. 4a). M8 events
295 usually involve only one asperity while a synchronous failure of both asperities usually results
296 in the M9 events. Analogue earthquakes are always followed by afterslip lasting for not more
297 than one frame (0.1 s) surrounding the asperities (Figure 3 a, b). Generally the shallow
298 asperity generates more surface displacement than the deep one: This is related to static
299 effects as predicted by elastic dislocation modelling (Figure A1). The picture inverts when the
300 correction for depth of dislocation is applied. Then, deeper asperities show larger slip. This is
301 consistent with higher loads causing higher frictional strength at greater depth as predicted by
302 Mohr-Coulomb theory. As a consequence, the deeper asperities are mechanically stronger and
303 able to accumulate more slip deficit in the interseismic period compared to the shallow
304 asperities.

305 We refer to slip events which occur on both asperities within one time frame (0.1 s) as double
306 or synchronized events. If the second event occurs independently within the next frame, we
307 refer to it as an aftershock or a clustered event. A minority of aftershocks are actually
308 relatively small normal faulting events. We interpret those as a result of dynamic overshoot
309 during the preceding thrust event. Normal events occur almost exclusively in the shallow
310 asperity. We include those rare normal events in our analysis since they represent an integral
311 part of the long-term slip budget. Accordingly, they show up with a negative seismic moment
312 in Figure 4a.
313

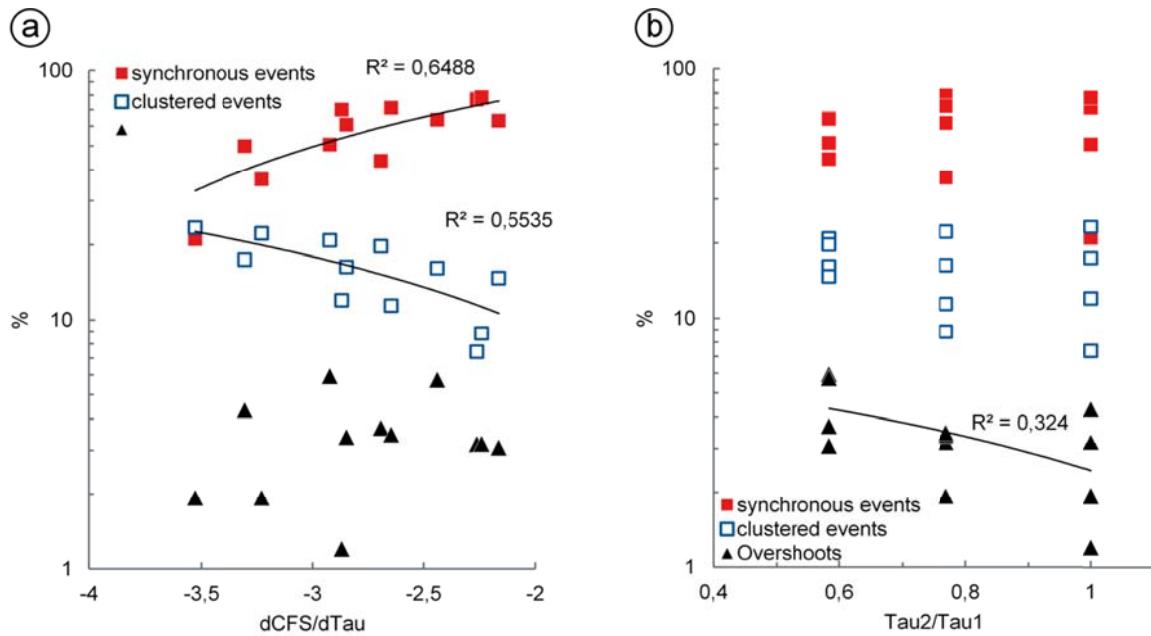


314

315 **Figure 4:** Example of an earthquake sequence simulated using seismotectonic scale modelling and
 316 derived by the numerical FEM-BV approach (all parameters scaled to nature): (a) event catalogue:
 317 (b) pdf of moment magnitude M_w , (c) pdf of recurrence time T_{rec} . See appendix figure A3 for pdfs of
 318 all experiments.

319 When analyzing synchronous (double) events, clustered (solo) events and normal events
 320 (overshoots) as a function of stress coupling $dCFS/d\tau$ and strength contrast τ_2/τ_1 a
 321 clear picture emerges (Figure 5). Accordingly, a synchronous double events increase in
 322 number from 20 to 80 % as stress coupling increases by two orders of magnitude (from less
 323 than a ppm up to a percent). At the same time, clustered events decrease. This simply reflects
 324 a higher degree of synchronization in strongly coupled systems. Overshoots show no clear
 325 correlation with stress coupling but a negative correlation with strength contrast (Figure 5).
 326 This is consistent with overshoots occurring preferentially in shallow regions of the wedge.

327 Both synchronous double and clustered solo events show no correlation with strength
 328 contrast. An apparent increase of the range of proportion of those events with stress contrast
 329 reflects the systematically wider range in stress coupling realized for lower strength contrasts.



330

331 **Figure 5:** Percentage of different types of events versus stress coupling (a) and strength contrast (b).

332 3.2 Frequency-size distributions

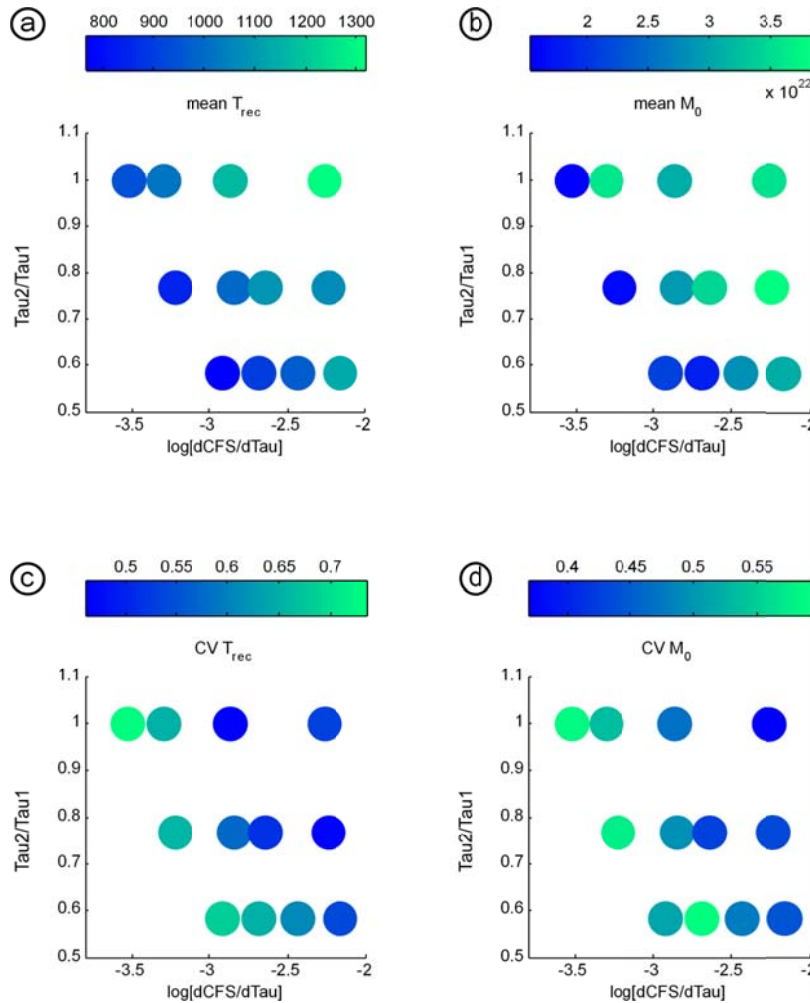
333 Frequency-size distributions of simulated earthquakes share similar shapes. The pdfs of
 334 moment magnitude are generally skewed negatively (towards the left) and very peaked as
 335 exemplified in Figure 4b. The PDFs of recurrence times are generally bimodal characterized
 336 by a peak at short periods (0.1 sec or 25 years) and a quasi-normally distributed bump around
 337 the mean recurrence time as exemplified in figure 4c.

338 Plotting mean recurrence times and mean seismic moments and their variability in terms of
 339 CV into the parameter space (Figure 6) shows the following: Mean recurrence time and
 340 seismic moment both increase with an increase in stress coupling. At the same time their CVs

341 decrease. R^2 -values for these correlations range between 0.3 and 0.6 (Table A1 in appendix)
342 and the trends considered significant.

343 We interpret this correlation of M_0 and T_{rec} with stress coupling as reflecting a dynamic
344 interaction causing higher slip in case of more strongly coupled asperities. Larger slip
345 consistently lengthens the interseismic period resulting in longer recurrence times. The
346 increase in size seems also to have a positive effect on the periodicity with larger stress drops
347 regulating the earthquake cycle thus decreasing the CV to 0.5.

348 A weak positive correlation exist between T_{rec} and strength contrast ($R^2 = 0.25$). Accordingly,
349 earthquake frequency increases as the weak asperity becomes weaker. We interpret this as
350 being a behavior predicted by Ruff (1996) where the weaker asperity, which has intrinsically
351 the shorter recurrence time, causes clock advance of the stronger asperity, which has
352 intrinsically longer recurrence times. A correlation between M_0 as well as the associated CVs
353 with strength contrast have not been observed to be statistically significant ($R^2 < 0.05$).



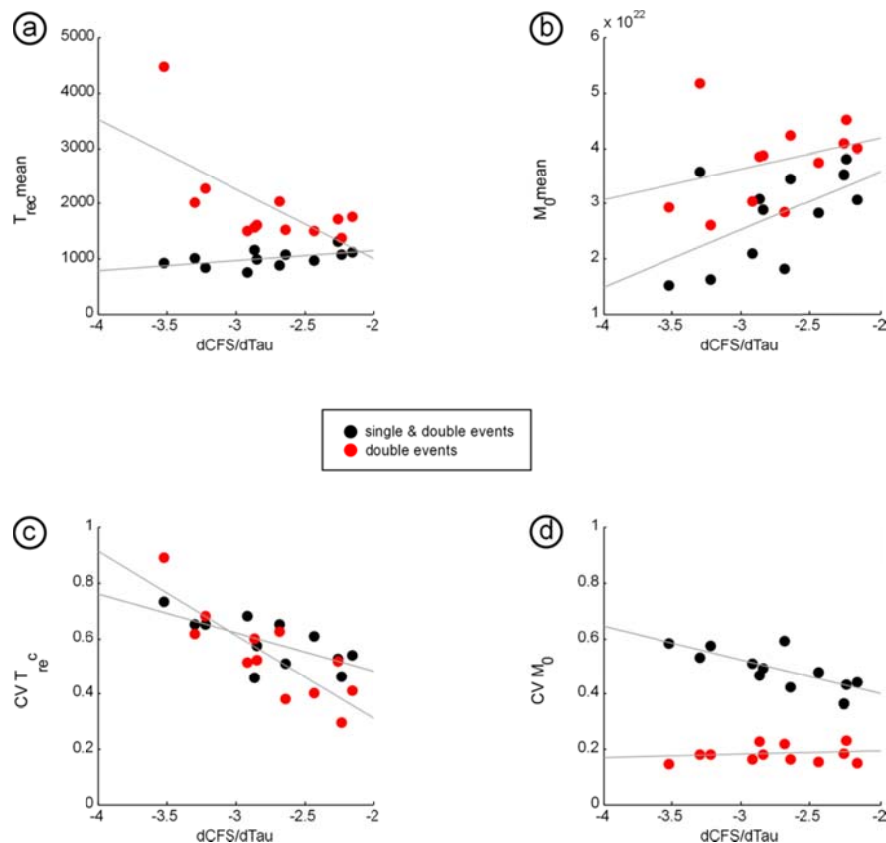
354

355 **Figure 6:** Correlation between of recurrence time (a, c) and seismic moment (b, d) with stress coupling
 356 ($dCFS/d\tau$) and strength contrast (τ_2/τ_1). See table A1 for regression analysis results.

357 The significant trends of M_0 and T_{rec} with $dCFS/d\tau$ are replotted in Figure 7 with a
 358 differentiation between all events (solo and double events) and solo events to explore the
 359 effects of stress coupling on the frequency-size distributions in more detail. Consistently,
 360 considering only double events increases mean seismic moment and mean recurrence time
 361 and decreases the associated CVs. This is simply a result of setting a magnitude threshold.

362 More interestingly, however, is the observation that the trends differ for the two groups of
 363 events: For example, the positive correlation of T_{rec} with stress coupling observed for all
 364 events is inverted to a negative correlation if only double events are considered (Fig. 7a). This
 365 is simply the result of double events being systematically rarer in more weakly coupled

366 systems as has been predicted by Ruff (1996). At the same time, recurrence times of double
 367 events are more sensitive to stress coupling than the recurrence times of all events: Double
 368 events recur almost randomly for weakly coupled systems and periodically for strongly
 369 coupled systems as suggested by a CV of T_{rec} ranging between 1 and 0.1. On the other side,
 370 the CV of M_0 is much smaller (0.2) and independent of stress coupling indicating a
 371 characteristic size of double events.



372

373 **Figure 7:** Correlation between of recurrence time (a) and its CV (c) and seismic moment (b) its CV (d) with
 374 stress coupling ($dCFS/d\tau$) for all events (black dots) and double events (red dots).

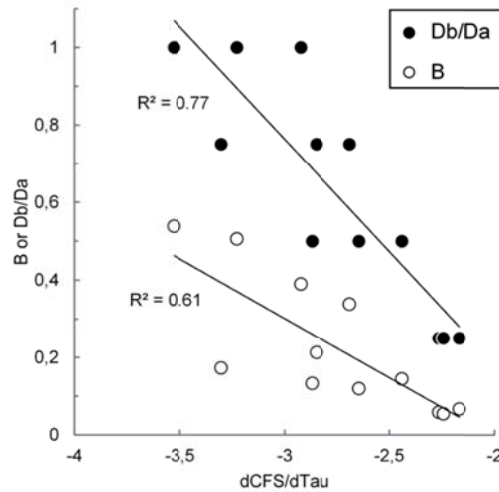
375 4 Discussion: Proxies for barrier efficiency

376 We simulated long time-series of analogue earthquakes in subduction zones in order to
 377 constrain the recurrence pattern emerging in a simple system with two asperities. Similar
 378 experiments (Corbi et al. 2017) and numerical simulations (Kaneko et al 2010) have been

379 carried out to find the critical parameters controlling the probability of a rupture bridging the
380 barrier and causing synchronized failure of the asperities. We here add experimental data
381 representing a different set of material parameters and geometries which allows testing the
382 existing concepts and to identify the minimum set of parameters needed.

383 Kaneko et al. (2010) suggested a set of parameters combined in a proxy for barrier efficiency
384 called B. B is the ratio of the stress increase required to bridge the barrier to the coseismic
385 stress drop. B included parameters which are directly and indirectly (involving assumptions)
386 observable in nature (geometric and friction parameters). Given the complexity of B and the
387 uncertainty in the choice of some of the parameters included (e.g. frictional parameters),
388 Corbi et al. (2017) aimed at a more simple proxy based solely on first-order geometric
389 relationships easy to observe in nature, i.e. the barrier-to-asperity length ratio D_b/D_a . With
390 respect to these two proxies, we consider the stress coupling as defined here as a proxy for
391 barrier efficiency of intermediate complexity. Similar to D_b/D_a it can be inferred primarily
392 from geometric observations (size and location of asperities), however, accounting for the
393 non-linear distribution of stress changes similar to B.

394 In Figure 8 we compare the three proxies based on the setup presented in this study.
395 Obviously, there is a good correlation between stress coupling, B and D_b/D_a . D_b/D_a seems
396 slightly more sensitive to stress coupling than is B as suggested by the steeper slope of
397 $D_b/D_a(dCFS/d\tau)$ in this plot. In any case, a correlation coefficient (R^2) of 0.6 to 0.8
398 suggests general interoperability of the three proxies.



399

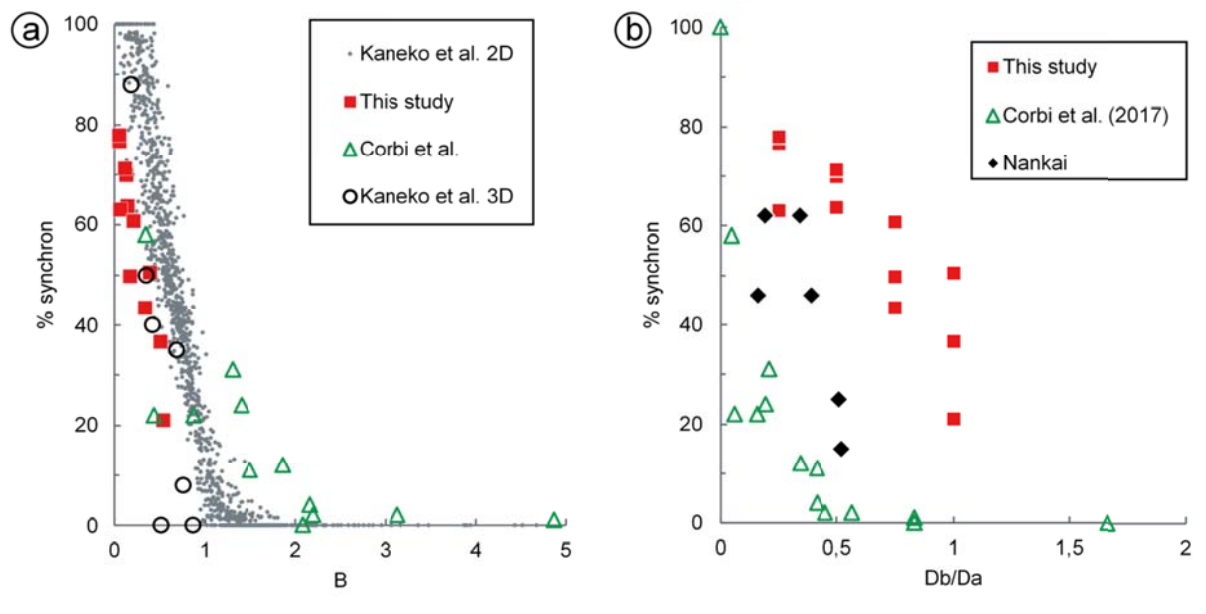
400 **Figure 8:** Correlation of stress coupling stress coupling with B and Db/Da parameters.

401 Figure 9 shows the collapse of all existing experimental, numerical and real world data in a
 402 plot of percentage synchronized ruptures (double events) versus B while plotting those data
 403 against Db/Da separates the data into roughly parallel trends. Because the data used represent
 404 a wide spectrum of geometrical and rheological parameters, the collapse indicates the
 405 versatile nature of the proxy B for anticipating double events.

406 On the other hand, the systematic offset trends suggest that while Db/Da seems to allow for a
 407 strong control on synchronization, material properties cannot be neglected. For instance, it
 408 appears that the setup used in the present study generates double events more easily. While
 409 for the experiments by Corbi et al. (2017) and the natural example a threshold for double
 410 events at Db/Da of 0.5 emerges, in the experiments presented here this threshold is
 411 significantly higher (>1). This suggests that the barrier in the Corbi et al. (2017) experiments
 412 as well as in the Nankai area are mechanically more effective than in our setup.

413 We conclude that for the moment being, the full complexity of the proxy B by Kaneko et al.
 414 (2010) is needed to account for the variability of mechanical parameters present in the

415 experiments. To which extent these parameters vary in nature and therefore control the
 416 threshold value of Db/Da remains to be explored.



417

418 **Figure 9:** Probability of synchronous events as a function of B (a) and Db/Da (b). Note collapse of experimental,
 419 natural and numerical simulation data in (a). Parallel offset trends in (b) are interpreted as due to differences in
 420 frictional properties between the experiments and nature.

421 5 Conclusions

422 Based on experiments generating long analogue earthquake time-series we explored the
 423 process of synchronization in a subduction zone megathrust setting with two velocity-
 424 weakening asperities separated by a velocity-strengthening barrier. We found the following:

- 425 • Synchronization is controlled by the static stress transfer from a one asperity to the
 426 other, quantified by the stress coupling $dCFS/s\tau$. Accordingly, the percentage of
 427 synchronized events scales with the logarithm of (normalized) Coulomb stress change
 428 on the receiver asperity.

- 429 • A strength contrast between the two asperities has no significant effect on
430 synchronization but decreases the recurrence time of double events because the
431 weaker asperity dictates the recurrence intervals.
- 432 • Analogue earthquakes in strongly coupled systems recur more periodically and with a
433 more characteristic size than in weakly coupled systems.

434 Three proxies for the barrier efficiency, B (Kaneko et al. 2010), Db/Da (Corbi et al., 2017)
435 and the newly defined stress coupling have been cross-validated and tested for
436 applicability:

- 437 • Db/Da is the most simple and easiest to apply proxy and incorporates the most
438 sensitive parameters to work first-order. It relies on geometries which – if they are
439 stationary over multiple seismic cycles - we are able to constrain using interseismic
440 locking and paleoseismological observations.
- 441 • B is the most versatile proxy and it captures the physics - but several parameters are
442 not well constrained or uncertain in nature.
- 443 • Stress coupling is of intermediate complexity and interoperable with Db/Da and B .

444 In order to arrive at a minimum set of parameters necessary to describe seismic hazard in
445 subduction zones we suggest to further explore the variability of those parameters in B
446 which are not well known in nature, to define the sensitivity of simpler proxies and to aim
447 at constraining their upper and lower bounds.

448 **Acknowledgements**

449 This study has been partially funded by the German Research Foundation (DFG)
450 collaborative research center SFB1114 “Scaling Cascades in Complex Systems”, project B01.

451 FC received funding from the European Union's Horizon 2020 research and innovation
452 program under the Marie Skłodowska-Curie grant agreement 658034 (AspSync).
453

454 **References**

- 455 Adam, J., O. Oncken, N. Kukowski, J. Lohrmann, S. Hoth, J. L. Urai, W. van der Zee, J.
456 Schmatz, B. Wieneke, and K. Pfeiffer (2005), Shear localisation and strain distribution during
457 tectonic faulting - New insights from granular-flow experiments and high-resolution optical
458 image correlation techniques, *Journal of Structural Geology*, 27(2), 183-301,
459 doi:10.1016/j.jsg.2004.08.008.
- 460 Caniven, Y., Dominguez, S., Soliva, Roger., Cattin, R., Peyret, M., Marchandon, M. Romano,
461 C, Strak, V. (2015). A new multilayered visco-elasto-plastic experimental model to study
462 strike-slip fault seismic cycle. *Tectonics*, 34, 232-264, doi:1002/2014TC003701.
- 463 Yannick Caniven, Stéphane Dominguez, Roger Soliva, Michel Peyret, Rodolphe Cattin,
464 Frantz Maerten, (2017), Relationships between along-fault heterogeneous normal stress and
465 fault slip patterns during the seismic cycle: Insights from a strike-slip fault laboratory model,
466 In *Earth and Planetary Science Letters*, Volume 480, Pages 147-157, ISSN 0012-821X,
467 <https://doi.org/10.1016/j.epsl.2017.10.009>.
- 468 Corbi, F., F. Funiciello, M. Moroni, Y. van Dinther, P. M. Mai, L. A. Dalguer, and C.
469 Faccenna (2013), The seismic cycle at subduction thrusts: 1. Insights from laboratory
470 models, *J. Geophys. Res. Solid Earth*, 118, 1483–1501, doi:10.1029/2012JB009481.
- 471 Corbi, F., F. Funiciello, S. Brizzi, S. Lallemand, and M. C. G. L. Rosenau (2017): Control of
472 asperities size and spacing on seismic behavior of subduction megathrusts, *Geophys. Res.*
473 *Letters*, 44,
- 474 Franzke, C., O'Kane, T., Monselesan, D., Risbey, J. and Horenko, I. (2015), Systematic
475 Attribution of Secular Southern Hemispheric Circulation Trends with Observational Forcing
476 Data, *Nonlin. Proc. Geophys.*, 22: 513-525.

- 477 Horenko, I. (2009), On robust estimation of low-frequency variability trends in discrete
478 Markovian sequences of atmospheric circulation patterns. *J. of Atmos. Sci.*, 66(11):1941-
479 1954.
- 480 Horenko, I. (2010), Finite element approach to clustering of multidimensional time series.
481 *SIAM J. of Sci. Comp.*, 32(1):62-83.
- 482 Hubbert, M. K. (1937), Theory of scale models as applied to the study of geological
483 structures, *Geological Society America Bulletin*, 48, 459-1520.
- 484 Kaiser, O. Igdalov, D. and Horenko, I. (2015), “Statistical regression analysis of threshold
485 excesses with systematically missing covariates.” *SIAM Multiscale Modeling & Simulation*
486 (*SIAM MMS*) , 13(2):594-613.
- 487 O’Kane, T. , Risbey, J. ,Monselesan, D., Horenko, I. and Franzke, C. (2016), “On the
488 dynamics of persistent states and their secular trends in the waveguides of the southern
489 hemisphere troposphere.” *Climate Dynamics* , 46(11-12):3567-3597.
- 490 Risbey, J., O’Kane, T., Monselesan, D, Franzke, C. and Horenko, I. (2015), “Metastability of
491 Northern Hemisphere teleconnection modes.” *J. Atmos. Sci.*, 72:35-54.
- 492 Kaneko, Y., J. P. Avouac, and N. Lapusta (2010), Towards inferring earthquake patterns from
493 geodetic observations of interseismic coupling, *Nature Geoscience*, 3(5), 363-U324,
494 doi:10.1038/ngeo843.
- 495 King, G. C. P., R. S. Stein, and J. Lin (1994), Static stress changes and the triggering of
496 earthquakes, *Bulletin of the Seismological Society of America*, 84(3), 935-953.

- 497 Kuehn, N. M., S. Hainzl, and F. Scherbaum (2008), Non-Poissonian earthquake occurrence in
498 coupled stress release models and its effect on seismic hazard, *Geophys. J. Int.*, 174, 649–658,
499 doi:10.1111/j.1365-246X.2008.03835.x.
- 539 Lin, J., Stein, R.S. (2004), Stress triggering in thrust and subduction earthquakes and stress
540 interaction between the southern San Andreas and nearby thrust and strike-slip faults, *Journal*
541 *of Geophysical Research*, 109, doi:10.1029/2003JB002607.
- 542 Metzner, P Putzig, L. and Horenko, I. (2012) “Analysis of persistent non-stationary time
543 series and applications.” *Comm. in Appl. Math. and Comp. Sci. (CAMCoS)*, 7(2):175-229.
- 544 Okada, Y. (1985), Surface deformation due to shear and tensile faults in a half-space, *Bulletin*
545 *of the Seismological Society of America*, 75(4), 1135-1154.
- 546 Okada, Y. (1992), Internal deformation due to shear and tensile faults in a half-space, *Bulletin*
547 *of the Seismological Society of America*, 82(2), 1018-1040.
- 548 Rosenau, M., F. Corbi, and S. Dominguez (2017), Analogue earthquakes and seismic cycles:
549 Experimental modelling across timescales, *Solid Earth*, 8, 3, 1-65, doi.: 10.5194/se-8-597-
550 2017
- 551 Rosenau, M., J. Lohrmann, and O. Oncken (2009), Shocks in a box: An analogue model of
552 subduction earthquake cycles with application to seismotectonic forearc evolution, *Journal of*
553 *Geophysical Research-Solid Earth*, 114, 20, doi: 10.1029/2008jb005665.
- 554 Rosenau, M., R. Nerlich, S. Brune, and O. Oncken (2010), Experimental insights into the
555 scaling and variability of local tsunamis triggered by giant subduction megathrust
556 earthquakes, *Journal of Geophysical Research-Solid Earth*, 115, doi:10.1029/2009jb007100.

- 557 Rosenau, M., and O. Oncken (2009), Fore-arc deformation controls frequency-size
558 distribution of megathrust earthquakes in subduction zones, *Journal of Geophysical Research-*
559 *Solid Earth*, 114, 12, doi:10.1029/2009jb006359.
- 560 Ruff, L. J. (1996), Large Earthquakes in Subduction Zones: Segment Interaction and
561 Recurrence Times, in *Subduction Top to Bottom*, edited, pp. 91-104, American Geophysical
562 Union.
- 563 Scholz, C. H. (1998), Earthquakes and friction laws, *Nature*, 391, 37-42.
- 564 Shearer, P.M., Stark, P.B. (2012), Global risk of big earthquakes has not recently increased,
565 *Proceedings of the National Academy of Sciences of the United States of America*, 109 (3),
566 pp. 717-721. DOI: 10.1073/pnas.1118525109
- 567 Shreve, R. L., and Cloos, M. (1986), Dynamics of sediment subduction, melange formation,
568 and prism accretion, *Journal of Geophysical Research*, 91, 10229 –10245.
- 569 Toda, S., Stein, R. S. (2002), Response of the San Andreas fault to the 1983 Coalinga-Nuñez
570 Earthquakes: An application of interaction-based probabilities for Parkfield, *Journal of*
571 *Geophysical Research*, 107, doi:0.1029/2001JB000172.
- 572 Vercauteren, N., Klein, R. (2015). A clustering method to characterize intermittent bursts of
573 turbulence and interaction with submeso motions in the stable boundary layer. *J. Atmos. Sci.*,
574 72, 1504-1517
- 575

576 Tab. A1

577

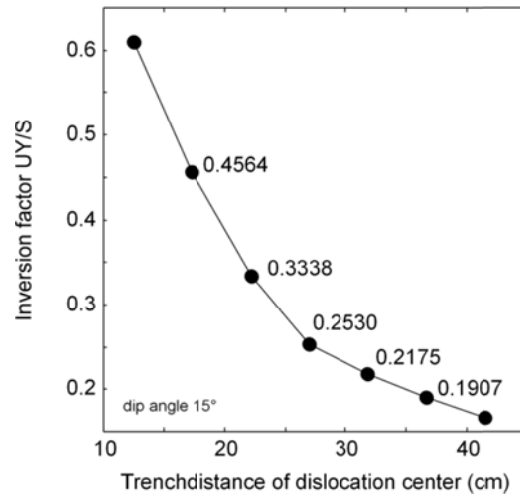
Parameter X	Parameter Y	R²
<i>dCFS/DTau</i>	T_{rec}	0.285
<i>dCFS/DTau</i>	M_0	0.333
<i>dCFS/DTau</i>	$CV T_{rec}$	0.475
<i>dCFS/DTau</i>	$CV M_0$	0.588
<i>Tau1/Tau2</i>	T_{rec}	0.245
<i>Tau1/Tau2</i>	M_0	0.055
<i>Tau1/Tau2</i>	$CV T_{rec}$	0.012
<i>Tau1/Tau2</i>	$CV M_0$	0.010

578

579 **Table A1:** Results from linear regression analysis (green = statistically significant; red = insignificant).See

580 Figure 6 for visualization of trends.

Fig. A1

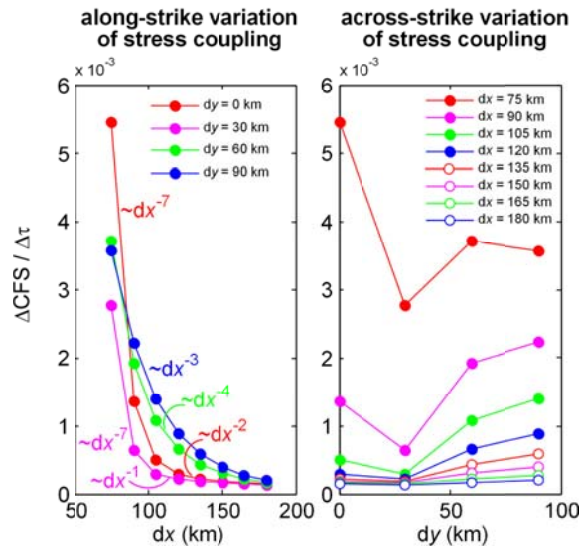


581

582 **Figure A1:** Relation between horizontal surface displacement and slip on dislocation as a function of trench

583 distance (depth).

Fig.A2

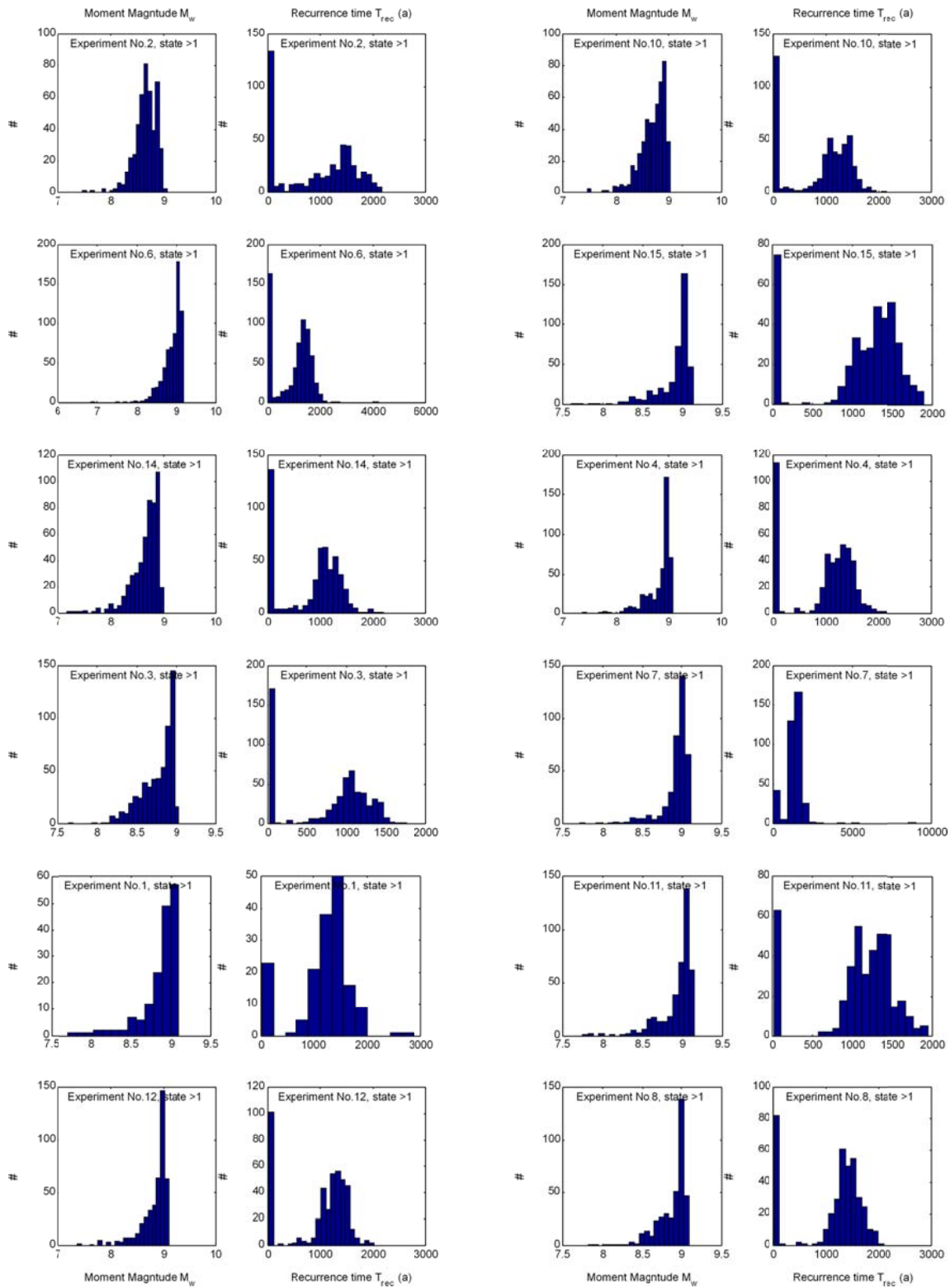


584

585 **Figure A2:** Spatial variation of coulomb stress transfer along strike and across strike of the subduction zone as

586 predicted by elastic dislocation modelling. Definition of dx and dy see main text.

Fig. A3



587

588 **Figure A3:** Probability distribution functions (pdfs) of M_w and T_{rec} for all experiments. The order of the plots
 589 is such that in the two rows experiments increase in stress coupling downwards. Second row is continuation of
 590 first row.